JOURNAL OF SPACECRAFT AND ROCKETS
Vol. 43, No. 3, May–June 2006

# Numerical and Experimental Investigation of PRORA USV Subsonic and Transonic Aerodynamics

R. Savino* and D. Paterna*
*University of Naples "Federico II," 80125 Naples, Italy*
and
M. Serpico†
*Italian Aerospace Research Center, 81043 Capua, Italy*

**The Italian unmanned space program PRORA USV (Programma di Ricerca Aerospaziale Unmanned Space Vehicle) is a technological program focused on the realization of flying test beds to demonstrate key vehicle and operational technologies applicable to future reusable launch vehicles. In this framework, the dropped transonic flight test is the first in a series of flight experiments the objective of which is the investigation of the final transonic part of the orbital return phase of a winged reentry vehicle. To prepare this mission, the development of the aerodynamic database is in progress, using both extensive wind tunnel tests and computational fluid dynamics. This study deals with investigations focused on the aerodynamic characterization of vehicle rudders in subsonic and transonic regimes for different angles of attack and rudder deflections. The aerodynamic characteristics of the vehicle are computed and discussed. Comparisons between numerical and available experimental data show a satisfactory agreement.**

## Nomenclature

| | | |
|---|---|---|
| $A$ | = | reference area, $m^2$ |
| $C$ | = | coefficients of the discretized momentum equation |
| $C_a$ | = | axial force coefficient |
| $C_D$ | = | drag coefficient |
| $C_f$ | = | skin friction coefficient |
| $C_L$ | = | lift coefficient |
| $C_{mx}$ | = | rolling-moment coefficient |
| $C_{my}$ | = | pitching-moment coefficient |
| $C_{mz}$ | = | yawing-moment coefficient |
| $C_P$ | = | pressure coefficient |
| $C_y$ | = | side-force coefficient |
| $C_z$ | = | normal force coefficient |
| $F$ | = | numerical convective flux of momentum, $kg \cdot m^{-1} \cdot s^{-2}$ |
| $L$ | = | reference length, m |
| $M$ | = | Mach number |
| $p$ | = | pressure, Pa |
| $Q$ | = | source term of the discretized momentum equation |
| $Re$ | = | Reynolds number |
| $T$ | = | temperature, K |
| $u$ | = | velocity component, m/s |
| $\alpha$ | = | angle of attack, deg |
| $\delta$ | = | rudder deflection angle, deg |
| $\rho$ | = | density, $kg \cdot m^{-3}$ |
| $\Omega$ | = | volume centered around a face, $m^3$ |

*Subscripts*

| | | |
|---|---|---|
| $i$ | = | generic momentum equation |
| $j$ | = | computational face |
| $l$ | = | left |
| $P$ | = | cell center |
| $r$ | = | right |
| $T$ | = | test section |

*Superscripts*

| | | |
|---|---|---|
| $*$ | = | approximate velocity field |
| $'$ | = | correction term |
| $m$ | = | iteration number |

## I. Introduction

THE Italian PRORA USV (Programma di Ricerca Aerospaziale Unmanned Space Vehicle) is a technology program oriented toward the maturation of selected technologies deemed necessary for the development of future generations of reusable access-to-space transportation systems. It has the aim of integrating with in-flight testing the already available capabilities at the Italian Aerospace Research Center (CIRA) with both theoretical–numerical analysis and on-ground experimental testing–validation. The technologies developed in the frame of the PRORA USV program will be necessary to successfully build and operate reusable space transportation systems with significantly lower cost of access to space; advanced thermal protection system, innovative aerothermodynamic design, and intelligent and integrated health management systems are some of the key technologies that will be demonstrated in the frame of the PRORA USV program.[1–3]

To achieve these objectives, different flight missions have been foreseen, ranging from transonic to hypersonic orbital reentry missions.

A schematic representation of the USV technology demonstrator, designed to perform the first transonic mission, is shown in Fig. 1. The USV geometric characteristics are reported in Table 1. It has full-span split elevons that, deflected symmetrically, provide pitch control, whereas asymmetric deflections provide roll control. It also features two symmetric vertical tails, with movable rudders, for directional stability/control.

The mission profile considered in this paper corresponds to the dropped transonic flight test; see Fig. 2. For the transonic mission, the USV vehicle will be released by a balloon at an altitude of about 24 km; the unpowered USV vehicle will accelerate up to transonic regime where specific flight experiments will be addressed to perform in-flight aerodynamic investigation. Drop tests are expected to be performed at the end of year 2006.

The CIRA Research Center is involved in the development of the preflight aerodynamic database of the vehicle. Wind-tunnel tests, including ground effect tests, have been conducted at subsonic and transonic speeds in the PT1 transonic wind tunnel. The wind-tunnel model is a 1:30 scaled version of the full size vehicle.

Received 24 March 2005; revision received 27 July 2005; accepted for publication 27 July 2005. Copyright © 2005 by the American Institute of Aeronautics and Astronautics, Inc. All rights reserved. Copies of this paper may be made for personal or internal use, on condition that the copier pay the $10.00 per-copy fee to the Copyright Clearance Center, Inc., 222 Rosewood Drive, Danvers, MA 01923; include the code 0022-4650/06 $10.00 in correspondence with the CCC.

*Research Scientist, Department of Space Science and Engineering "L. G. Napolitano."
†Research Engineer, Aerothermodynamics Section.

**Table 1 USV geometric parameters**

| Parameter | Value |
|---|---|
| *Full-scale geometric parameters* | |
| Total length, m | 8.00 |
| Wing span, m | 3.56 |
| Fuselage planform area, $m^2$ | 6.70 |
| Wing planform area, $m^2$ | 3.74 |
| Total planform area, $m^2$ | 10.44 |
| Base area, $m^2$ | 0.72 |
| Nose radius, m | 0.010 |
| Wing leading edge radius, m | 0.010 |
| Sweepback wing angle 1, deg | 45 |
| Sweepback wing angle 2, deg | 76 |
| Dihedral angle, deg | 5 |
| *Full-scale reference parameters* | |
| Reference length, m | 1.05 |
| Reference area, $m^2$ | 3.60 |
| Aspect ratio (wing) | 3.39 |

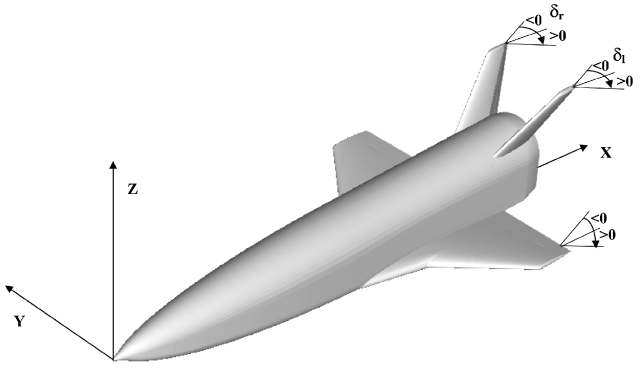


**Fig. 1 USV geometry, coordinate system, and control surface deflection.**

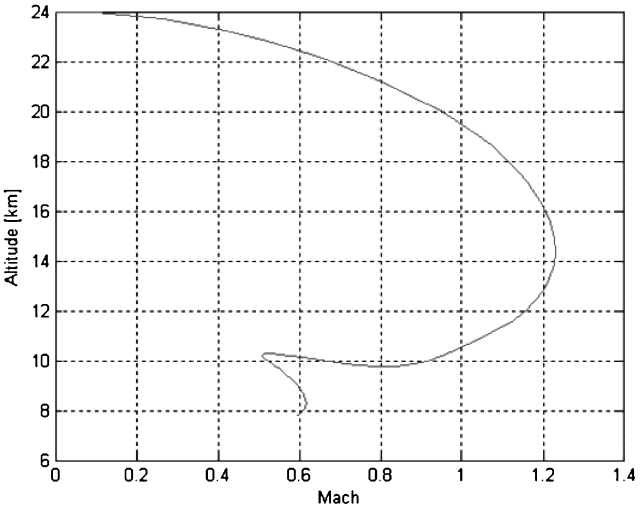


**Fig. 2 USV dropped transonic flight test trajectory.**

The computational fluid dynamics simulations presented in this paper were performed at the Department of Space Science and Engineering of the University of Naples "Federico II," including the variation of aerodynamic coefficients from wind-tunnel to full-scale flight conditions. The activities include code validation, grid generation, grid convergence study, and analysis of the results. The test matrix of the computations is shown in Table 2. The total number of simulated conditions is 40, 36 corresponding to free-flight and 4 to wind-tunnel conditions. The free-flight cases differ by altitude (Mach and Reynolds numbers), angle of attack (0, 5, 10 deg), and rudder deflection (5, 10, 20 deg). The rudders are deflected asymmetrically. Wind-tunnel conditions correspond to two Mach numbers ($M = 0.5$, $M = 1.05$) and two angles of attack ($\alpha = 0$ deg, $\alpha = 10$ deg). In these cases, the rudders are deflected symmetrically ($\delta = \pm 10$ deg).

**Table 2 Computational matrices for rudder efficiency**

| Mach | *Re* | AOA, deg | | | $\delta$, deg | | |
|---|---|---|---|---|---|---|---|
| | | *Free-flight conditions* | | | | | |
| 0.5 | 1.2e5 | 0 | 5 | 10 | 0 | 5 | 10 |
| 0.7 | 6.39e5 | 0 | 5 | 10 | 0 | 5 | 10 |
| 0.9 | 3.36e6 | 0 | 5 | 10 | 0 | 5 | 10 |
| 1.05 | 4e6 | 0 | 5 | 10 | 0 | 5 | 10 |
| | | *Wind-tunnel conditions* | | | | | |
| 0.5 | 6.17e5 | 0 | 10 | | 10 | −10 | |
| 1.05 | 9.3e5 | 0 | 10 | | 10 | −10 | |

The objective of this paper is to present an overview of the rudder efficiencies of the USV vehicle in the transonic regime, discuss the main results, and compare with experimental results.

Laterodirectional stability and related control problems have not been addressed in the present article. However, as far as laterodirectional analysis is concerned,[4] results indicate that equilibrium in sideslip flight can always be attained with the present rudder configuration. The critical parameter for stability can be identified in the location of the vehicle center of mass, which strongly influences the dynamic of roll during actuation of rudders.[4]

## II. Numerical Model

### A. Numerical Code

The numerical code uses the finite-volume method to solve Reynolds-averaged Navier–Stokes (RANS) equations in an unstructured grid, following a cell-centered approach.

The numerical algorithm is based on the SIMPLE (semi-implicit method for pressure-linked equations) scheme.[5] All the unknown variables are computed at the center of each computational cell (colocated approach). The momentum equation is linearly approximated as

$$C_p u_i^{*m} + \sum C_j u_{ij}^{*m} = Q_i^{m-1} - \left(\frac{\partial p}{\partial x_i}\right)_P^{m-1} \tag{1}$$

where the coefficients $C$ and $Q$ depend on the type of discretization. In particular, the convective fluxes are computed according to a deferred correction approach[6]:

$$F_j = \dot{m}_j u_{i,j}^{\mathrm{UD}(m)} + \dot{m}_j \left(u_{i,j}^{\mathrm{CD}(m-1)} - u_{i,j}^{\mathrm{UD}(m-1)}\right) \tag{2}$$

where the superscript UD (upwind differencing) denotes a first-order upwind approximation to $u_i$ at the generic cell face, and CD (central differencing) represents a second-order central approximation. If the numerical solution converges, the first and third terms in Eq. (2) cancel, so that the final converged solution is second-order accurate. In this way, only the simpler upwind term is treated implicitly, allowing an easier solution of the linear system of Eq. (1). The diffusive fluxes are computed using central schemes, taking into account the grid nonuniformity, and treating implicitly only the terms that are closer to the cell center $P$.[6] System (1) is solved by using an algebraic multigrid method.[7] The solution of system (1) does not satisfy continuity, because the pressure gradient term is evaluated at the previous step. Therefore, a correction to the velocity field is needed that, according to the SIMPLE family of algorithms, is approximated as a function of the pressure gradient:

$$u_j' = -\Omega_j \overline{\left(\frac{1}{C_p}\right)} \left(\frac{\partial p'}{\partial x}\right)_j \tag{3}$$

To avoid the numerical oscillations of the pressure field typical of a colocated grid arrangement, a special treatment of the pressure–velocity coupling is performed,[6] utilizing a linear interpolation [denoted by an overbar in Eq. (3)] for the computation of the coefficients $C_P$.

Equation (3) is substituted in the continuity equation, and a Poisson-like equation for the pressure correction is obtained, which is again solved using the multigrid method. The continuity equation takes into account the compressibility effects. In particular, the density is written as the sum of two terms: the first, which does not satisfy the continuity equation, is used in Eq. (1); the correction term is used in the continuity equation and is written as a function of the pressure correction:

$$\rho' = p'/RT \tag{4}$$

where $T$ is the temperature evaluated at the previous iterative step.

Equations (3) and (4) are then used to compute the velocity correction. The resultant velocity field is inserted into the energy and turbulence equations, which are discretized and solved in a way similar to Eq. (1). The vehicle surface is assumed adiabatic. The $k$–$\varepsilon$ model of Shih et al.[8] is used, because it shows superior performance over the standard $k$–$\varepsilon$ model for largely separated flows. Wall functions are used for the turbulence treatment at walls.

It must be pointed out that the limitation of standard RANS models in application to massively separated flows is that these models are designed and calibrated for essentially attached flows, so that they should be tuned for each application involving flow separation. However, large eddy simulation of the turbulence is not currently feasible for a complete aircraft configuration, though also the more practical detached eddy simulation approach over complex configurations is still a challenge from a computational point of view.[9]

This procedure is repeated iteratively until a final converged solution for all variables is obtained.

All computations have been performed on a cluster of workstations. Each computational node is equipped with a 1.8-GHz Pentium processor and 768-MB memory modules. They are connected to each other with a 100-Mbit/s switch. Such a configuration allows simulations on grids of up to 5 million cells. The computational speedup (i.e., the ratio between the computational speed on $n$ processors and that of a single processor) is almost linear up to six processors.

As a preliminary validation, a test case consisting of a wing–body configuration at Mach and Reynolds numbers close to the ones used for the present simulations ($M = 0.75$, $Re = 3 \times 10^6$) has been selected. The geometry is the DLR-F4 wing–body, and experimental data are available from the National Aerospace Laboratory, ONERA, and the Defence Research Agency.[10] Figure 3 shows the wing–body polar. Agreement with the available experimental data is satisfactory.

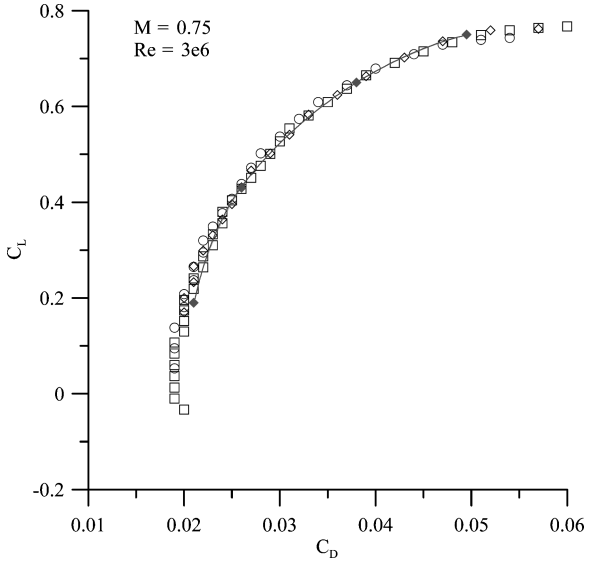


**Fig. 3 Validation of the numerical code: comparison of lift and drag coefficients: ◇, NLR-HST; □, ONERA-S2MA; ○, DRA; and ——, present computations ($k$–$\varepsilon$).**

In addition, to validate the code for the flight conditions investigated in this paper, some of the computations have also been carried out using the zonal euler Navier–Stokes parallel flow solver,[11] available at CIRA, capable of solving the compressible RANS equations around complex aeronautical configurations using multiblock structured grids. In this code, numerical discretization is based on a second-order cell-centered finite volume method with explicitly added (fourth-order) dissipation. The unsteady solution procedure is based on the dual time-stepping method, where a pseudo-steady-state problem is solved at each time step. Conventional convergence accelerators, including geometrical multigrid and residual smoothing, are used. The code, written with vectorial technology, has been extensively used to simulate flowfields around and in complex geometries[12,13] on the new NEC SX-6 supercomputer.

For numerical simulations selected for the present computations, the standard $k$–$\varepsilon$ turbulence model has been used. For the investigated conditions, good quantitative agreement was found between the two codes, in terms of flowfield distributions and overall aerodynamic coefficients. Only a few results are reported in Table 3, which refers to the normal force coefficient and to the pitching moment coefficient at different Mach numbers, and 10 deg of angle of attack. Additional data can be found in Refs. 14–16.

### B. Computational Grid

Figure 4 shows the computational grid corresponding to 3.6 million cells. The $x$ axis is the longitudinal axis, the $z$ axis is orthogonal to the $x$ axis and lies in the vehicle symmetry plane, and the $y$ axis completes the right-handed orthogonal coordinate system.

The computational domain is subdivided into 150 blocks. Figure 5 shows the block distribution on the vehicle surface. The external boundary is positioned at about 10 body lengths in each direction, so that freestream conditions are correctly imposed. The coordinate $y^+$ of the first cells adjacent to the surface is about 10.

The computational grid used for wind-tunnel simulations is symmetrical, because for such a configuration the rudders are deflected symmetrically by an angle $\delta = \pm 10$ deg. It differs from the free-flight configuration due to the presence of a 25-cm-long sting, starting from the base of the vehicle. The total number of cells is about 3.2 million.

**Table 3 Comparison between present numerical code and ZEN code**

| Mach | AOA | $C_z$ (present code) | $C_z$ (ZEN code) | $C_{my}$ (present code) | $C_{my}$ (ZEN code) |
|---|---|---|---|---|---|
| 0.5 | 10 | 0.91 | 0.89 | −4.9 | −4.7 |
| 0.7 | 10 | 0.91 | 0.91 | −4.9 | −4.9 |
| 1.05 | 10 | 1.1 | 1.1 | −6.3 | −6.4 |

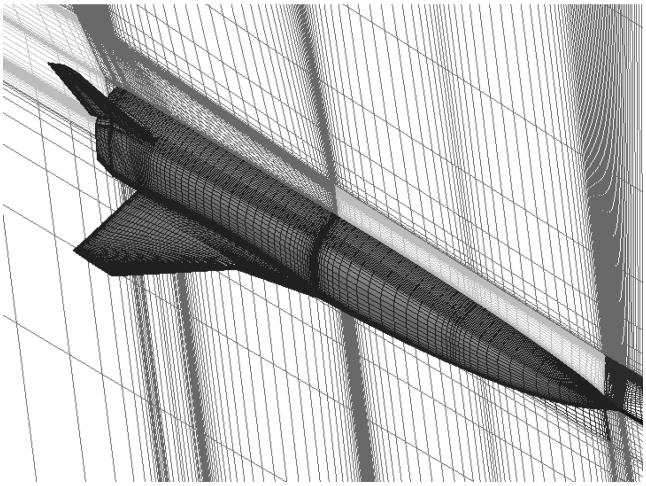

**Fig. 4 Computational mesh on the vehicle surface and on symmetry plane (3.6-million-cell grid).**

**Table 4 Aerodynamic coefficients comparison between two different grids (run C-VT-3, $M = 0.5$, $\alpha = 0$)[a]**

| Coefficient | 3.6 million | 4.2 million |
|---|---|---|
| $C_D$ | 0.106 | 0.110 |
| $C_L$ | 0.0243 | 0.0220 |
| $C_y$ | −0.121 | −0.118 |
| $C_{mx}$ | 0.107 | 0.108 |
| $C_{my}$ | 0.0357 | 0.0380 |
| $C_{mz}$ | −0.268 | −0.264 |

[a]Moments center: $x = 5.6$, $y = 0$, $z = -0.26$ m.

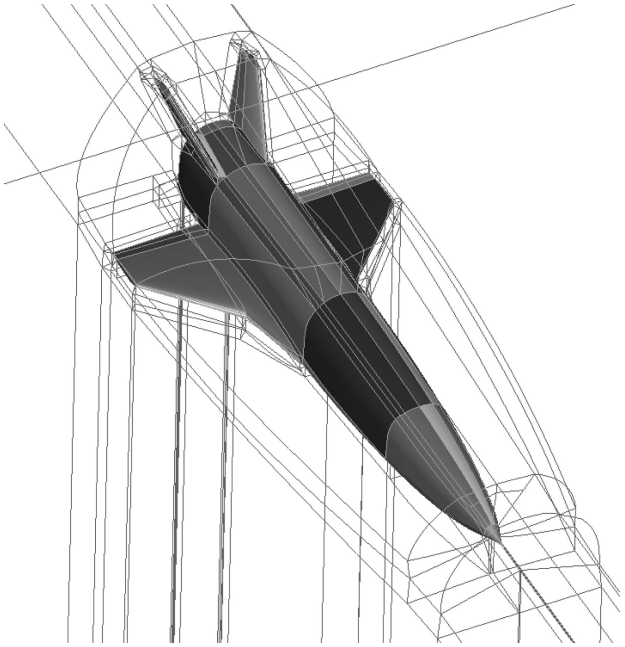

**Fig. 5 Grid block distribution.**

### C. Grid Convergence Analysis

Convergence criteria are based on the equation residuals and on the behavior of the global aerodynamic coefficients during the iterative process of the computational algorithm. Furthermore, some fluid-dynamic variables in the flowfield (pressure, Mach number) are monitored during iterations. A two-order-of-magnitude reduction of the residuals of the different equations (continuity, momentum, energy, turbulence) is typically obtained after 3000 iterations. Furthermore, force and moment coefficients reach an almost stationary value after about 2000 iterations. Thus, the numerical solution is considered converged after 3000 iterations.

A preliminary grid convergence analysis has been carried out on four different grids (1.4, 2.5, 3.6, and 4.2 million cells). Two different flight conditions have been examined, corresponding to Mach numbers $M = 0.5$ and 1.05, and a single geometrical configuration has been taken into account, corresponding to an asymmetrical rudder deflection of $\delta = 20$ deg.

Figures 6a and 6b show the lift and pitching moment grid dependence for $M = 0.5$. Major discrepancies are observed between the coarsest grid results (1.4-million-cell grid) and the other two grids. Aerodynamic coefficients exhibit variations not larger than 5% between the 2.5- and 3.6-million-cell grids.

Table 4 shows the results of the simulations at $M = 0.5$, $\alpha = 0$. In this case, the results from 3.6- and 4.2-million-cell grids are compared. The largest discrepancies are observed on lift coefficients, with differences, however, not exceeding 9%.

The pressure coefficient and skin friction profiles obtained from the computations on the 3.6 and 4.2 million-cell grids have been compared along different longitudinal sections and are in good agreement. They are not shown here for reasons of space.

In particular, stagnation values of the pressure coefficient and temperature are in good agreement with theoretical values. In conclusion, the convergence analysis has shown that the computational grid with 3.6 million cells is sufficiently accurate, and it has been used for all of the computations to be discussed.

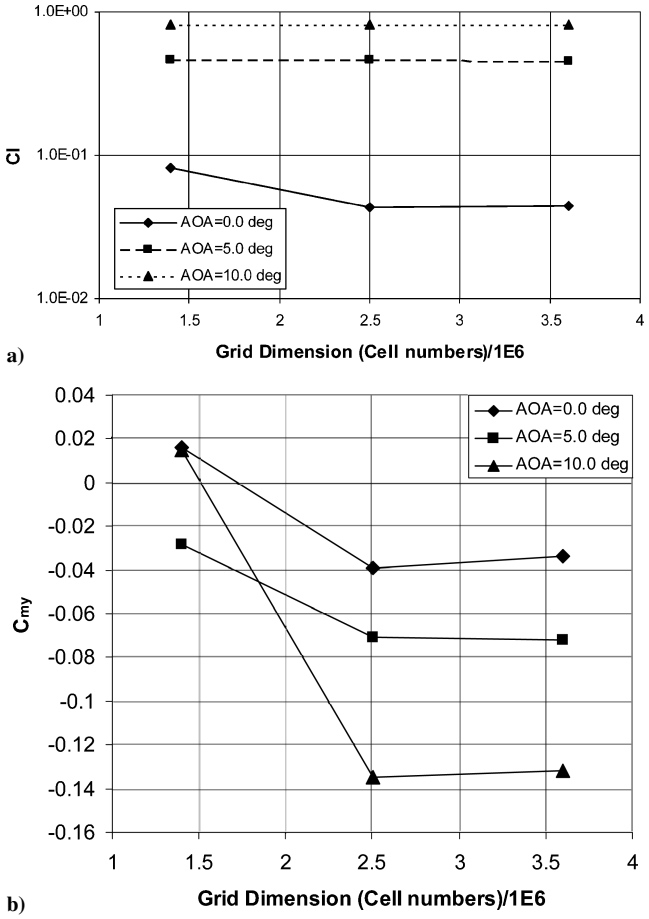


**Fig. 6 Grid convergence analysis: a) lift and b) pitching moment coefficient for grid independence ($M = 0.5$).**

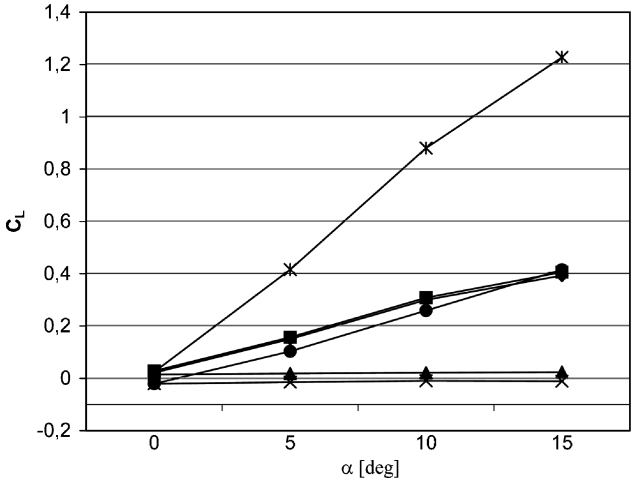


**Fig. 7 Variation of lift coefficient with angle of attack, and contributions from wing, tails, and fuselage ($M = 0.5$, $\delta = 20$ deg): ◆, right wing; ■, left wing; ▲, right tail; ×, left tail; ●, fuselage; and ✳, total.**

## III. Test Facility and Experimental Procedure

The transonic research tunnel PT-1 is a closed-circuit, pressurized wind tunnel in operation since September 1998. The facility is managed by the Aerodynamic Testing Laboratory within the Experimental Aerodynamics Department. The main mission of the facility is to support industrial and research program with a versatile and

high-flow-quality aerodynamic testing platform over a wide speed range, for two- and three-dimensional test articles. The facility is capable of both continuous operation in the low subsonic range ($M = 0.1$–$0.35$), through a 132-kW fan-drive system, and intermittent operation in the high subsonic–transonic range ($M = 0.35$–$1.1$) and supersonic (one point at $M = 1.4$), by means of an air-injection drive system (max flow rate 26 kg/s, max supply pressure 34 bar). The facility is equipped with two test sections, one for subsonic tests and the second for transonic/supersonic tests with perforated walls (60-deg inclined holes, 6.3% porosity). Both test sections have floor and ceiling adjustable walls ($\alpha = \pm 0.5$ deg).

The facility was equipped with the porous test chamber, with a modified porosity distribution optimized for wall interference reduction.

The model was equipped with a 0.150-mm transition grit placed at 35% of the chord on the wing upper side and at 50% of the chord on the lower side, around the body at 20% of the length of the model, and finally on the vertical tails at 25% of tail chord for the outer surface and at 45% of chord for the inner surface. The model was also equipped with two cavity pressure taps that allow the calculation of the forebody aerodynamic coefficients.[17,18]

Freestream pressure $P_T$ is measured by the wind-tunnel data system using a United Sensor-type pitot tube installed in the settling chamber. The sensor has a diameter of 0.25 in., a 45-deg convergent inlet, and a length of 24 in. The pressure range is 1 to 2 bar.

The pressure is acquired by a RUSKA 6222 absolute transducer with a full scale of 26 PSI and an accuracy of 0.01% full scale (FS). This device is used to obtain an accurate calculation of the Mach number and to provide a highly accurate reference pressure for all values measured as differential pressure.

Forces and moments acting on the model during tests are measured by a three-component balance via the MGC Plus system. The full scales of the balance are normal force = 1500 N, axial force = 240 N, and pitching moment = 60 Nm. The accuracy is 0.29% FS for normal force, 0.4% FS for axial force and 0.37% FS for pitching moment.

To take into account the base effects it was necessary to measure cavity pressure in the model. This was acquired at two pressure taps

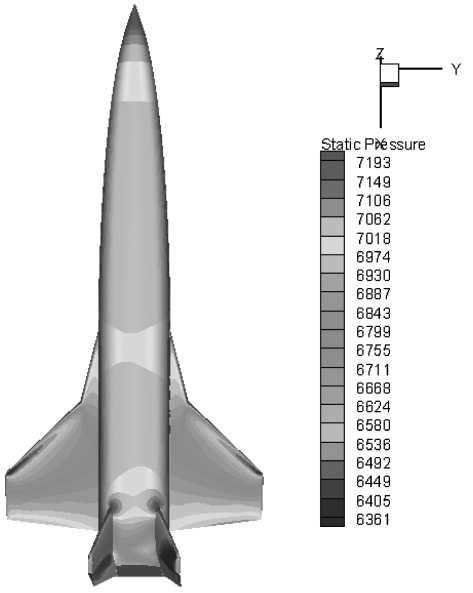


**Fig. 8 Pressure distribution on the upper vehicle surface, $M = 0.5$, $\alpha = 0$.**

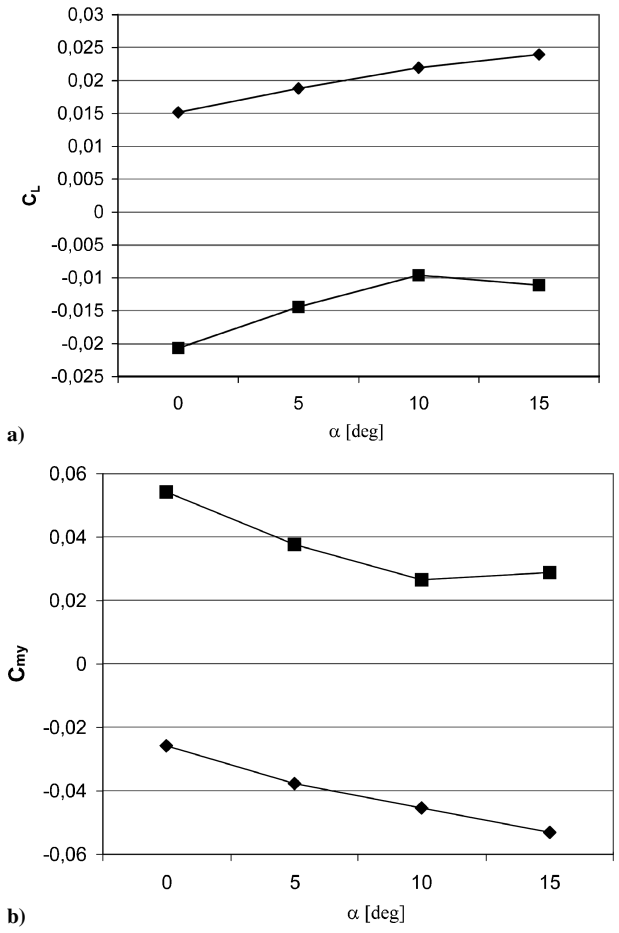


**Fig. 9 Tail contributions to a) lift coefficient and b) pitching moment coefficient for $M = 0.5$, $\delta = 20$ deg; ◆, right tail and ■, left tail.**

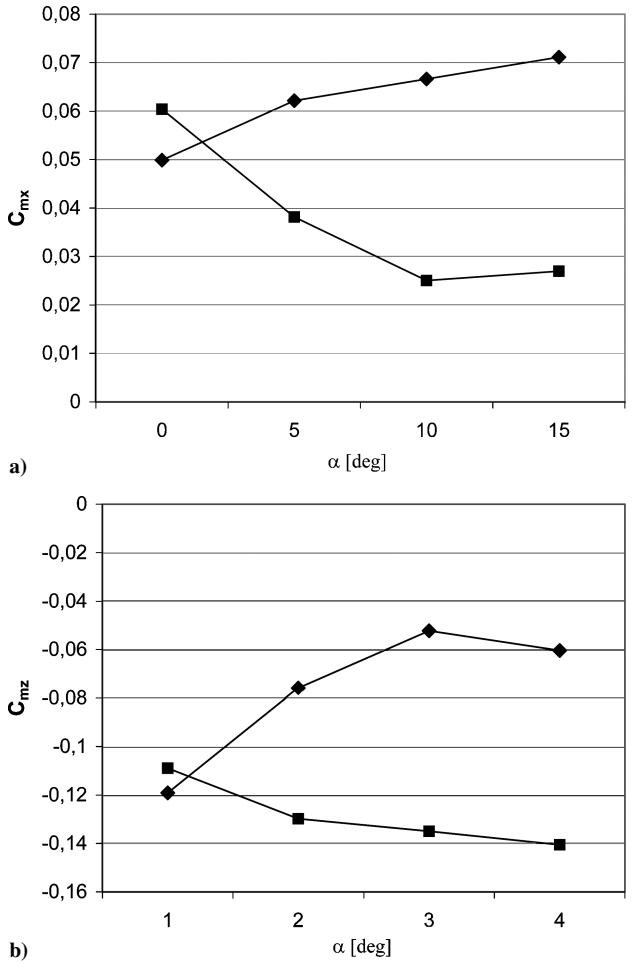


**Fig. 10 Tail contributions to a) rolling moment coefficient and b) yawing moment coefficient for $M = 0.5$, $\delta = 20$ deg: ◆, right tail and ■, left tail.**

positioned well inside the model and was measured as differential from reference static pressure by a PSI 8400 scanner, with a 5-psi FS and 0.05% FS accuracy transducer.

During tests the effective incidence was different from the nominal one reported in the test matrix. To take into account sting deflection during the run due to aerodynamic loads, this angle was corrected by an amount estimated comparing two snapshots of the model taken respectively during the run and before the run. Image processing was done by a MATLAB® code.[19] This method was used because it was not possible to install an inclinometer into the model. Model AOAs before the run were measured with a water level (whose accuracy was 30 arcseconds). Using this method the correct $\Delta\alpha$ for each run has been evaluated, the estimated accuracy being $\pm 0.05$ deg (Refs. 17 and 18).

The experimental procedure has been validated by using an AGARD-C calibration model[20] and different-sized delta-wing models. A comprehensive description of the validation activity may be found in Refs. 17 and 18.

## IV. Results and Discussion

Reference parameters for the computation of the aerodynamic coefficients are reported in Table 1. The moment center is the vehicle center of gravity ($x = 5.6$ m, $y = 0$, $z = -0.26$ m for the full-size vehicle).

The different contributions to the aerodynamic coefficients due to fuselage, wings, and vertical tails are computed separately. Each calculation is split, in turn, into its pressure and viscosity contributions.

### A. Effects of the Angle of Attack and Mach Number ($\delta = 20$ deg)

The effect of the angle of attack on the lift coefficient is shown in Fig. 7 ($M = 0.5$, $\delta = 20$ deg). The lift coefficient is almost linear up to $\alpha = 10$ deg; then, between $\alpha = 10$ and $\alpha = 15$ deg, the lift-curve slope decreases. Vertical tail contribution to lift is negligible, whereas the fuselage provides a contribution comparable with that of the wing.

Pressure distribution on the upper vehicle surface is shown for $M = 0.5$ and $\alpha = 0$ deg in Fig. 8. Vertical tail contribution to lift is shown in Fig. 9a. Because the deflection of the rudders is asymmetrical, contributions to the lift coefficient have opposite signs, and, in particular, while the right tail ($y < 0$) has positive lift, the left one has negative lift. Figure 9a also shows that when the angle of attack increases, the lift contribution of the vertical tails increases.

Correspondingly, the contribution to the pitching moment coefficient from the left tail is positive, whereas the right tail has a negative contribution (Fig. 9b).

In contrast, the rolling and yawing moment coefficients from the vertical tails have the same sign. However, the variations of these coefficients with the angle of attack behave in the opposite way (Figs. 10a and 10b).

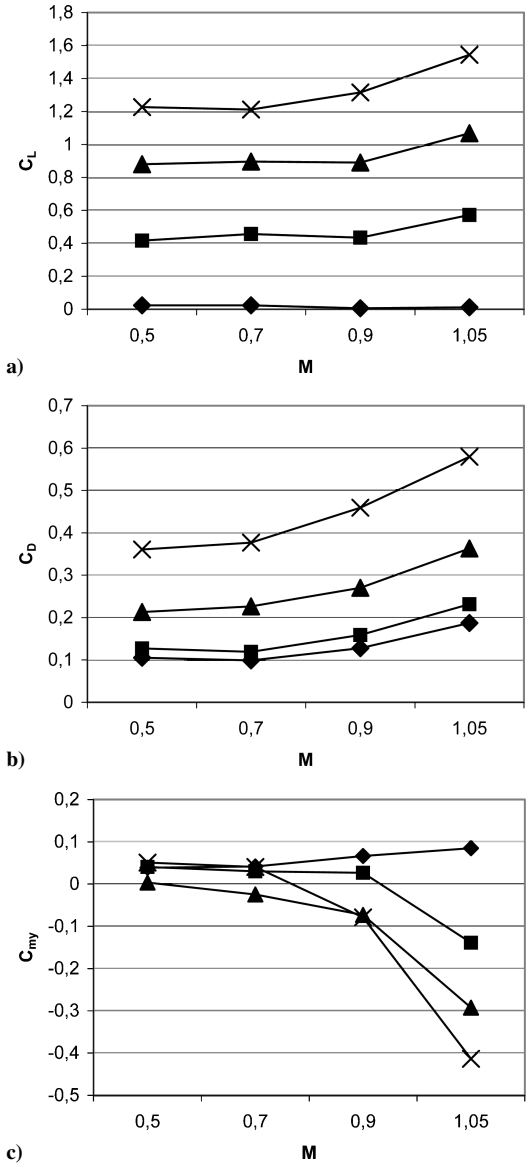


**Fig. 11 Variation of aerodynamic coefficients with Mach number ($\delta = 20$ deg): ◆, $\alpha = 0$; ■, $\alpha = 5$; ▲, $\alpha = 10$; and ×, $\alpha = 15$.**

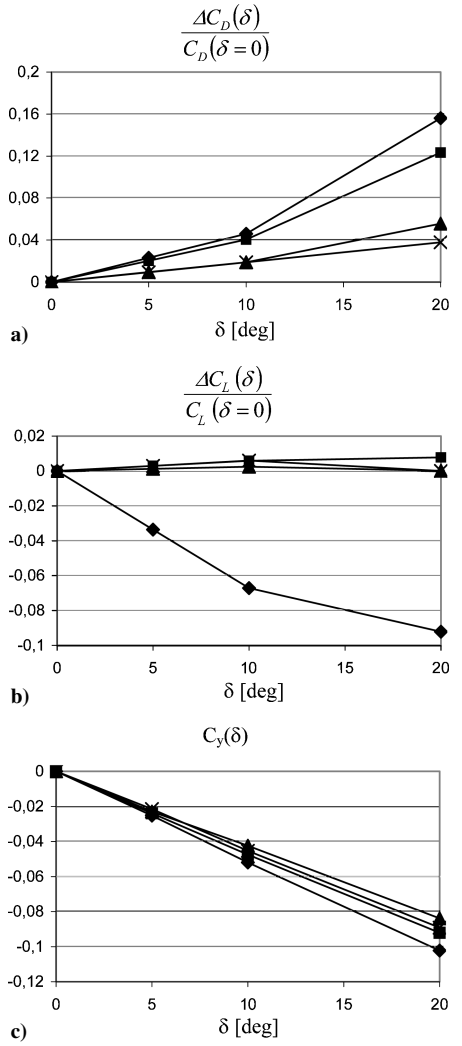


**Fig. 12 Variations of a) drag, b) lift, and c) side-force coefficients with rudder deflection angle $\delta$ for $M = 0.5$ deg: ◆, $\alpha = 0$; ■, $\alpha = 5$; ▲, $\alpha = 10$; and ×, $\alpha = 15$.**

The aerodynamic coefficients for the flight conditions at $M = 0.7$, 0.9, and 1.05 in Table 2a exhibit similar trends. In particular, drag coefficients at $M = 0.7$ are slightly lower than the corresponding values at $M = 0.5$. This behavior is due to the different Reynolds numbers corresponding to the two flight conditions: $Re = 1.2 \times 10^6$ at $M = 0.5$ and $Re = 6.4 \times 10^6$ at $M = 0.7$.

Figures 11a–11c summarize the variation of the lift, drag, and pitching moment coefficients with the Mach number. For a prescribed value of $\alpha$, aerodynamic coefficients show a rise with the maximum value at Mach 1.05.

### B. Comparison of Different Flight Configurations: Rudder Efficiency

This paragraph describes the results related to the three different rudder deflection angles (5, 10, 20 deg) for all flight conditions of Table 2. In particular, increments of aerodynamic coefficients due to rudder deflection have been determined. Reference values ($\delta = 0$) for the calculation of the increments have been obtained by linearly extrapolating the results at $\delta = 5$ and $\delta = 10$ deg.

Figure 12a shows the increments of the tail drag coefficient at different angles of attack at $M = 0.5$. It may be observed that for all $\delta$, maximum incremental variations of the drag coefficients are obtained at $\alpha = 0$ deg, where drag is minimum and, therefore, $\Delta C_D / C_D$ maximum.

This is also the case for the lift coefficient, shown in Fig. 12b. Variations of the lift coefficient with the rudder deflection angle are negligible everywhere, except in the case $\alpha = 0$ deg, where $C_L$ is close to 0. Indeed, as stated above, an asymmetrical deflection of the rudders determines an increment of lift on the right tail and a decrement on the left tail, so that the global effect is negligible.

Figure 12c shows the increment of the side force coefficient with $\delta$. In this case, $\Delta C_y = C_y$, because for $\delta = 0$, $C_y = 0$. Linear behavior of the side force coefficient may be observed at all angles of attack. In particular, at $\alpha = 15$ deg, $C_y$ values are lower than the corresponding ones at $\alpha = 10$ deg, and this is most likely due to interference phenomena between the fuselage and the vertical tails. In this regard, Figs. 13a and 13b show pressure distributions on the tails at $M = 0.5$, $\delta = 20$ deg, for two different angles of attack ($\alpha = 10$ and 15 deg). Figure 13b shows that, at $\alpha = 15$ deg, the lower $C_Y$ depends both on the pressure decrease close to the root of the right tail and on the lower compression on the rudder of the left tail, which is partially shadowed by the fuselage.

Increments of the tail moment coefficients at $M = 0.5$ are shown in Figs. 14a–14c. The rolling moment coefficient ($C_{mx} = \Delta C_{mx}$) in Fig. 14a presents an almost constant slope at all angles of attack. Similar considerations hold for the yawing moment coefficient ($C_{mz} = \Delta C_{mz}$) (Fig. 14c). Variation of the incremental pitching moment coefficient (Fig. 14b) is nonnegligible only at $\alpha = 0$ deg, where $C_{my}$ is relatively small compared with other angles of attack.

The effect of the Mach number on increments of the side force and the rolling and yawing moment coefficients is shown in Figs. 15–17. Rudder efficiency is minimum at $M = 0.9$. Under this condition,

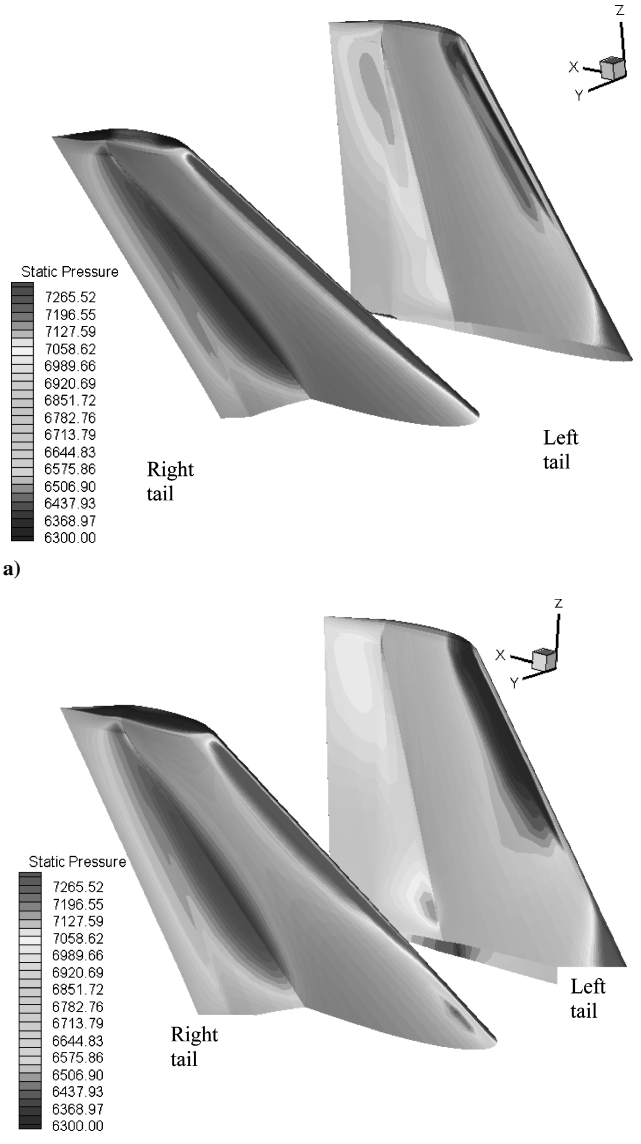


**Fig. 13 Pressure distribution (pascals) on vertical tails ($M = 0.5$, $\delta = 20$ deg); a) $\alpha = 10$ deg and b) $\alpha = 15$ deg.**

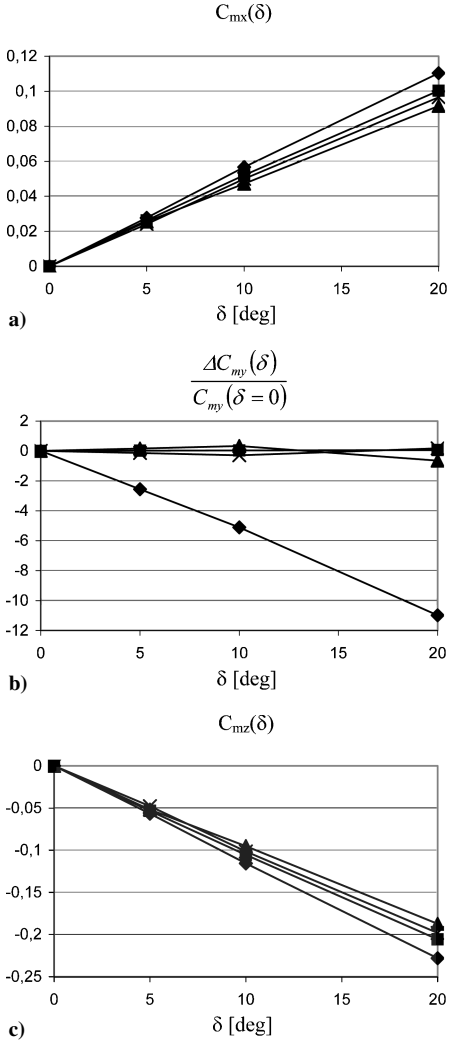


**Fig. 14 Variations of a) rolling, b) pitching, and c) yawing moment coefficients with rudder deflection angle $\delta$ for $M = 0.5$: ◆, $\alpha = 0$; ■, $\alpha = 5$; ▲, $\alpha = 10$; and ×, $\alpha = 15$.**

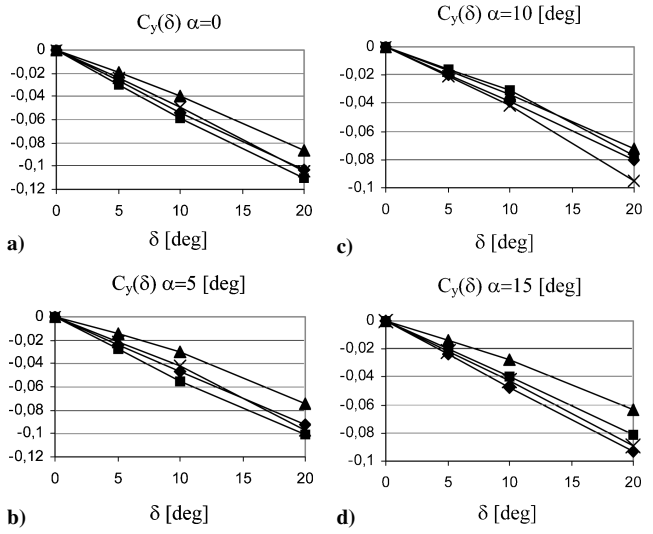


**Fig. 15 Variations of side force coefficient with $\delta$: a) $\alpha = 0$ deg, b) $\alpha = 5$ deg, c) $\alpha = 10$ deg, and d) $\alpha = 15$ deg: ◆, $M = 0.5$; ■, $M = 0.7$; ▲, $M = 0.9$; and ×, $M = 1.05$.**

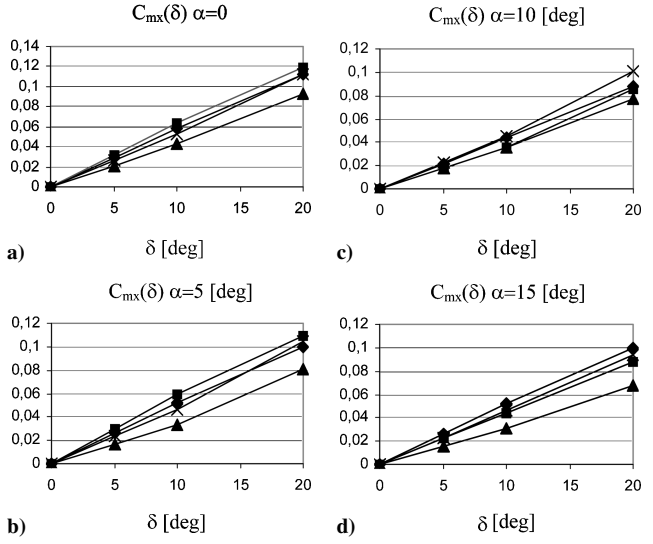


**Fig. 16 Variations of rolling moment coefficient with $\delta$: a) $\alpha = 0$ deg, b) $\alpha = 5$ deg, c) $\alpha = 10$ deg, and d) $\alpha = 15$ deg: ◆, $M = 0.5$; ■, $M = 0.7$; ▲, $M = 0.9$; and ×, $M = 1.05$.**

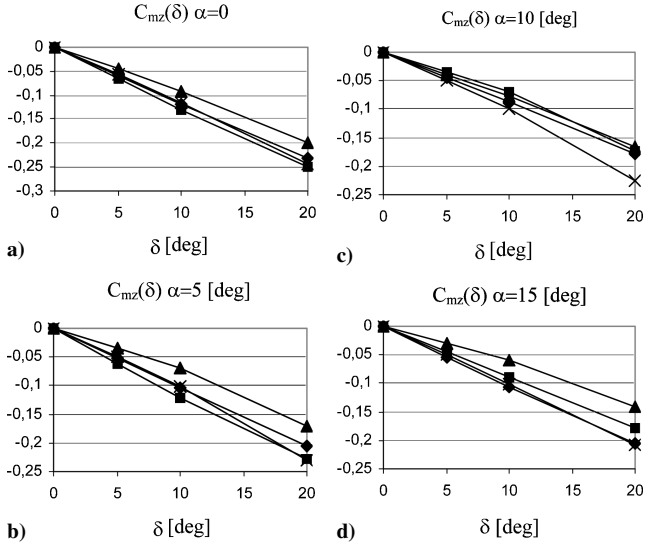


**Fig. 17 Variations of yawing moment coefficient with $\delta$: a) $\alpha = 0$ deg, b) $\alpha = 5$ deg, c) $\alpha = 10$ deg, and d) $\alpha = 15$ deg: ◆, $M = 0.5$; ■, $M = 0.7$; ▲, $M = 0.9$; and ×, $M = 1.05$.**

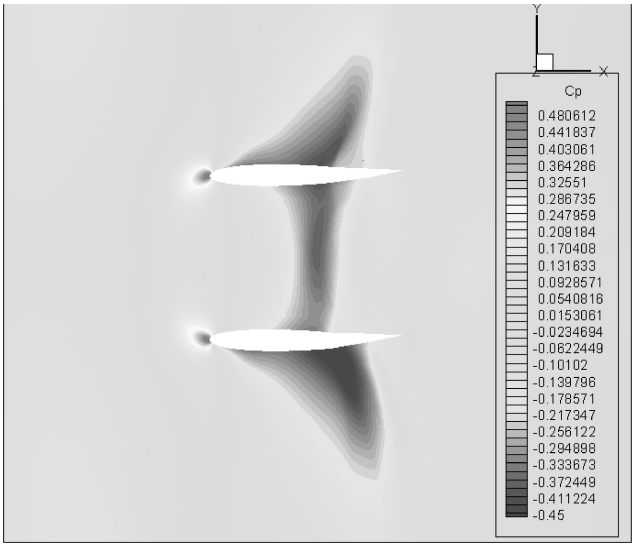


a)

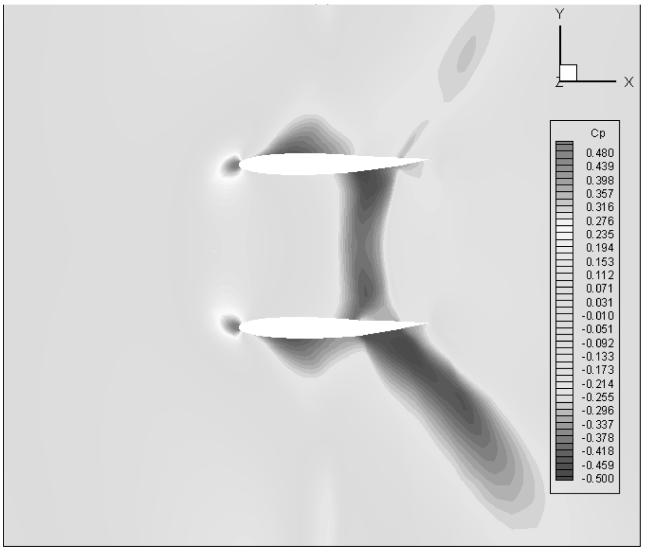


b)

**Fig. 18 Pressure coefficient in the plane $z = 0.5$ [m] for $\alpha = 0$ deg, $\delta = 5$ deg: a) $M = 0.9$ and b) $M = 1.05$.**

shock wave–boundary layer interactions are evident in the computations (Figs. 18a and 18b). Figure 18a shows the pressure coefficient distribution in the section $z = 0.5$ m, for $M = 0.9$, $\alpha = 0$ deg, $\delta = 5$ deg. A shock wave is present between the vertical tails. Shock waves are also present in the outer region, at about one-half of the rudder length. This shock-wave system induces a boundary layer separation. In the case $M = 1.05$ (Fig. 18b), the same shock wave moves forward, causing a different pressure distribution on the rudders.

### C. Wind-Tunnel Results and Comparison with Experimental Data

Because the wind-tunnel configuration is symmetrical, the attention has been focused only on lift, drag, and pitching moment coefficients.

The different contributions to the aerodynamic coefficients in free flight and wind-tunnel results at the same Mach number are shown in Table 5. It should be pointed out that free-flight computations and simulations of the wind-tunnel conditions, according to the wind-tunnel experiments, refer to different rudder deflections. To analyze the different contributions of the fuselage, wings, and rudders in symmetric and asymmetric configurations, and at different Reynolds numbers, all numerical results have been summarized.

Relative variations of lift coefficient with rudder deflection angle are not negligible, due to $C_L$, which is close to 0. The free-flight

**Table 5 Different contributions to lift and drag coefficients in free-flight and wind-tunnel conditions**

| | $M$ | AOA | $\delta_R$ | $\delta_l$ | $C_D$ | $C_L$ |
|---|---|---|---|---|---|---|
| Wind tunnel | 0.5 | 0 | 10 | −10 | 0.0711 | 0.0573 |
| Fuselage | | | | | 0.0467 | −0.00961 |
| Wing | | | | | 0.0133 | 0.0514 |
| Rudders (left and right) | | | | | 0.0111 | 0.0155 |
| Free flight | 0.5 | 0 | 10 | 10 | 0.0895 | 0.033 |
| Fuselage | | | | | 0.0574 | −0.0154 |
| Right wing | | | | | 0.0101 | 0.0245 |
| Left wing | | | | | 0.0105 | 0.0284 |
| Right rudder | | | | | 0.00545 | 0.00707 |
| Left rudder | | | | | 0.00615 | −0.0115 |
| Wind tunnel | 1.05 | 0 | 10 | −10 | 0.136 | 0.0324 |
| Fuselage | | | | | 0.0779 | −0.0311 |
| Wing | | | | | 0.0335 | 0.0674 |
| Rudders (left and right) | | | | | 0.025 | −0.00393 |
| Free flight | 1.05 | 0 | 10 | 10 | 0.154 | 0.0213 |
| Fuselage | | | | | 0.094 | −0.0283 |
| Right wing | | | | | 0.0176 | 0.0346 |
| Left wing | | | | | 0.0175 | 0.0346 |
| Right rudder | | | | | 0.0117 | −9.62e-4 |
| Left rudder | | | | | 0.0134 | −0.0186 |

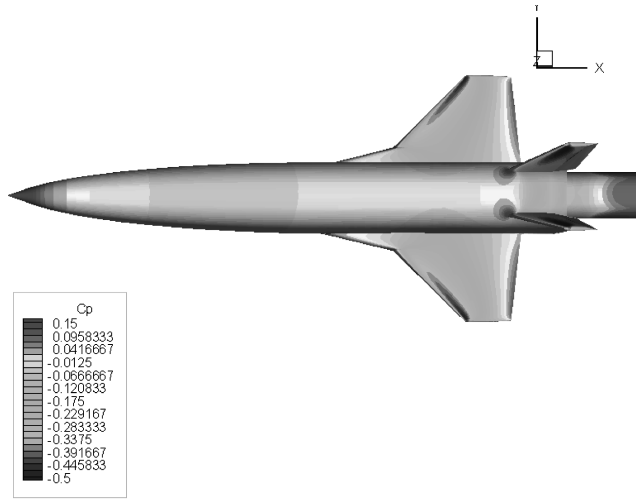


a)

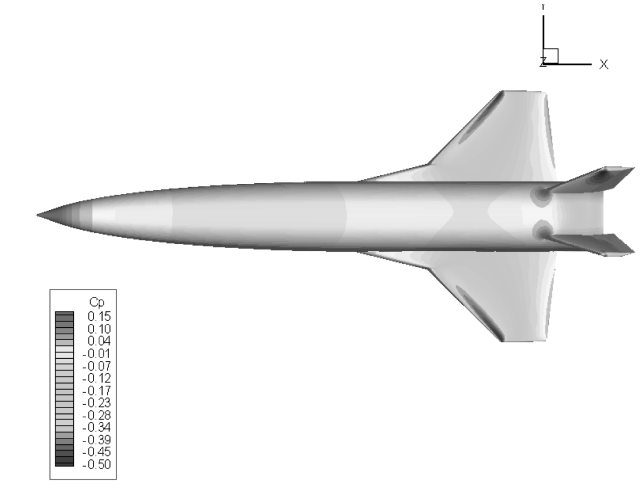


b)

**Fig. 19 Surface pressure coefficient for $M = 0.5$, $\alpha = 0$ deg: a) wind tunnel ($\delta = \pm 10$ deg) and b) free flight ($\delta = 10$ deg).**

drag coefficient is larger than the corresponding wind-tunnel value, both on the wing and on the fuselage. The larger contribution to the drag on the fuselage is mainly due to base drag, which is almost absent in the wind-tunnel model due to the presence of the sting.

Different $C_D$ values of the wing can be explained by a different pressure recovery on the wing trailing edge, caused by sting interference. This is clear in Figs. 19a and 19b, showing pressure coefficient distributions in free flight and in the wind tunnel ($M = 0.5$, $\alpha = 0$ deg).

Differences in lift coefficients are mainly due to the different rudder deflections (asymmetrical in free flight, symmetrical in wind tunnel), which determine a different pressure field on the fuselage. In the tunnel conditions the left tail is lifting; therefore the total lift coefficient is larger. Pitching moment coefficient contributions from wing and fuselage are comparable in both cases, whereas the different deflection of the left rudder determines a different global

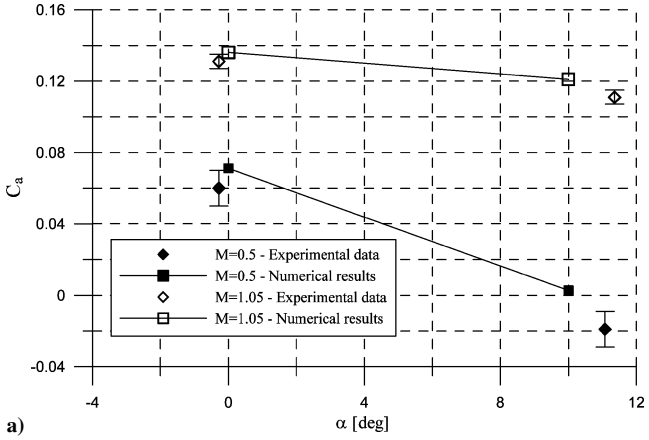


a)

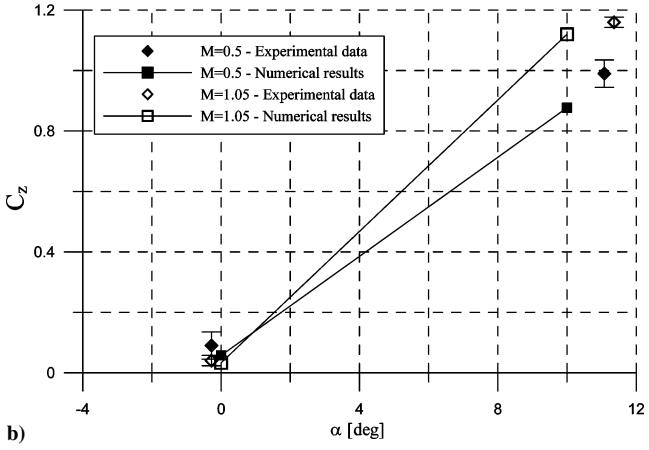


b)

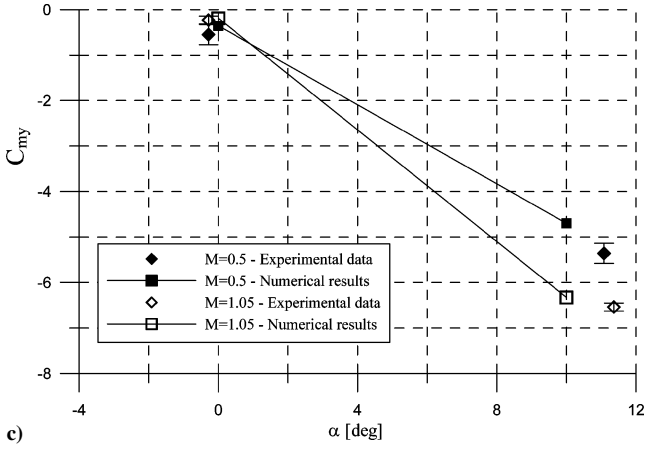


c)

**Fig. 20 Experimental–numerical comparison: a) axial force coefficient, b) normal force coefficient, and c) pitching moment coefficient.**

$C_{my}$. In particular, the pitching moment coefficient is positive in free-flight conditions, negative in wind-tunnel conditions. Comparing only the coefficients on the right tail in free-flight and wind-tunnel conditions, which are deflected by the same angle ($\delta = 10$ deg) on the same side, one finds sufficient agreement.

The same considerations hold for $M = 0.5$, $\alpha = 10$ deg. In this case, differences in the aerodynamic coefficients are even lower, because the different contribution of the left tail is an order of magnitude lower than the wing and fuselage contributions.

At $M = 1.05$ the differences between free-flight and wind-tunnel drag values are very low, and this can be explained by the fact that the sting disturbance cannot influence the wing. The fuselage drag is again larger in free flight, due to the base drag contribution. Global lift is larger in the wind tunnel case due to different left rudder deflection. Similarly, the pitching moment coefficient is larger in free flight, due to the different contribution of the left tail.

The comparison between computed and measured aerodynamic coefficients is shown in Figs. 20a–20c. In particular, Fig. 20a shows the axial force coefficient, Fig. 20b the normal force coefficient and Fig. 20c the pitching moment coefficient. Agreement between numerical and experimental results is satisfactory in both the subsonic ($M = 0.5$) and transonic ($M = 1.05$) regimes, especially considering the experimental uncertainties shown in Fig. 20.

## V. Conclusions

The effects of the angle of attack and Mach number on the aerodynamic coefficients of the USV vehicle have been determined for three flight configurations corresponding to different rudder deflection angles. Lift, drag, and pitching moment coefficients are quite similar for such configurations, because the rudders are deflected asymmetrically.

A larger satisfactory rudder deflection results mainly in an increment of the side force and of the rolling and yawing moments, at all angles of attack. The increment is linear with the deflection angle.

Results of the wind-tunnel simulations on a scaled USV model, even though the examined configuration is different from the free flight configurations, have confirmed the free-flight results and shown a slight interference, in subsonic conditions, with the sting mounted on the test model base.

Comparison between numerical and experimental aerodynamic coefficients is satisfactory in the analyzed range of Mach numbers, showing how current numerical methods are able to predict overall aerodynamic coefficients also in a critical transonic region.

## Acknowledgments

The authors thank the reviewers for useful remarks and suggestions.

## References

[1]Russo, G., and Capuano, A., "The PRORA-USV Program," *Proceedings of the 4th European Symposium on Aerothermodynamics for Space Vehicles*, SP 487, ESA, Noordwijk, The Netherlands, 2002, pp. 37–48.

[2]Russo, G., and Marino, G., "The USV Program and UHTC Development," *Proceedings of the 4th European Symposium on Hot Structures and Thermal Protection Systems for Space Vehicles*, SP-521, ESA, Noordwijk, The Netherlands, 2002, pp. 29–38.

[3]Marino, G., Russo, G., Denaro, A., and Borriello, G., "USV: Flying Test Bed Opportunity for TPS and Hot Structures," *Proceedings of the 4th European Symposium on Hot Structures and Thermal Protection Systems for Space Vehicles*, SP-521, ESA, Noordwijk, The Netherlands, 2002, pp. 139–146.

[4]"PRORA–USV FTB 1 Trimmability and Manoeuvrability Analysis," Centro Italiano Ricerche Aerospaziale, TN-03-283, Rev. 1, Capua, Italy, Sept. 2003.

[5]Patankar, S. V., *Numerical Heat Transfer and Fluid Flow*, Hemisphere, Washington, DC, 1980.

[6]Ferziger, J. H., and Peric, M., *Computational Methods for Fluid Dynamics*, 3rd rev. ed., Springer-Verlag, Heidelberg, Germany, 2002.

[7]Weiss, J. M., Maruszewski, J. P., and Smith, W. A., "Implicit Solution of Preconditioned Navier–Stokes Equations Using Algebraic Multigrid," *AIAA Journal*, Vol. 37, No. 1, 1999, pp. 29–36.

[8]Shih, T.-H., Liou, W. W., Shabbir, A., Yang, Z., and Zhu, J., "A New $k$–$\varepsilon$ Eddy-Viscosity Model for High Reynolds Number Turbulent Flows—Model Development and Validation," *Computers and Fluids*, Vol. 24, No. 3, 1995, pp. 227–238.

[9]Squires, K. D., Forsythe, J. R., Wurtzler, K. E., Strang, W. Z., Tomaro, R. F., Grismer, M. J., and Spalart, P. R., "Towards Prediction of Aircraft Spin," High Performance Computing User's Group Conf. 2001, June 2001.

[10]"A Selection of Experimental Test Cases for the Validation of CFD Codes," AGARD-AR-303, Vol. 2, Aug. 1994.

[11]Serpico, M., and Schettino, A., "Preliminary Aerodynamic Performance of the PRORA-USV Experimental Vehicle," *4th European Symposium for Space Vehicles*, SP 487, ESA, Noordwijk, The Netherlands, 2001, pp. 183–190.

[12]Iaccarino, G., Marongiu, C., Catalano, P., and Amato, M., "RANS Modeling and Simulations of Synthetic Jets," AIAA Paper 2004-2223, June 2004.

[13]Serpico, M., Schettino, A., Ciucci, A., Falconi, D., and Fabrizi, M., "Base Flow Predictions for a Lightsat Launcher at Supersonic Speeds," *Journal of Spacecraft and Rockets*, Vol. 36, No. 2, 1999, pp. 247–254.

[14]"Aerodynamic Database Development for PRORA-USV Programme: Rudders Efficiency—Zero Sideslip," Dept. of Space Science and Engineering, DISIS Internal Rept. 9, Univ. of Naples "Federico II," Naples, Italy, June 2003.

[15]"Aerodynamic Database Development for PRORA-USV Programme: Rudders Efficiency—No Zero Sideslip," Dept. of Space Science and Engineering, DISIS Internal Rept. 11, Univ. of Naples "Federico II," Naples, Italy, Nov. 2003.

[16]Rufolo, G., and Roncioni, P., "Aerodynamic Characterization and Aerodataset Development of the PRORA-USV Reusable Vehicle," AIAA Paper 2005-3406, May 2005.

[17]"USV Programme: Wind Tunnel Test Campaign on AGARD C Calibration Model," Centro Italiano Ricerche Aerospaziale, Internal Document CIRA-TRP-03-609, Capua, Italy, Rev. 0, 2003.

[18]"USV Programme: Wind Tunnel Test Campaign on Delta Wings for Wall Interference Assessment and Corrections in CIRA PT-1 Wind Tunnel," Centro Italiano Ricerche Aerospaziale, Internal Document CIRA-TRP-03-554, Capua, Italy, Rev. 0, 2003.

[19]"The MATLAB Language and How to Develop MATLAB Applications," MathWorks, 1994, URL: http://www.mathworks.com.

[20]Hills, R., "A Review of Measurements on a AGARD Calibration Model," AGARDograph 64, Nov. 1961.

R. Cummings
*Associate Editor*